Nonlinear Analysis of Oscillator Mutual Injection Locking Through Inductor Coupling

Almudena Suárez, *Fellow, IEEE*, Franco Ramírez, *Senior Member*, *IEEE*, and Robert Melville, *Senior Member, IEEE*

***Abstract*— This work presents an in-depth investigation of the nonlinear behavior of two mutually injection-locked oscillators through inductor coupling. An analytical formulation, solved through an innovative procedure, facilitates the understanding of the qualitative transformations in the system solutions when increasing the coupling factor. The analysis demonstrates that, in a manner similar to the unilaterally injection-locked oscillators, families of disconnected/connected curves are obtained when increasing this factor, although the patterns, associated with distinct operation modes, are more complex. Then, an accurate numerical method to predict the behavior of coupled transistor-based oscillators is presented, based on nonlinear admittance models of the individual oscillators. Mathematical conditions are derived to solve the coupled system through a two-level contour-intersection technique. In this way, all the solutions coexisting for a given set of element and parameter values are calculated simultaneously, in an exhaustive manner. The cases of two coupled oscillators at the fundamental frequency and at 1:3 frequency ratio are considered. Possible applications include the oscillator phase-noise reduction and the implementation of sensors using the phase shift between the two oscillator elements.**

***Index Terms*— oscillators, harmonic balance, stability analysis, phase-noise analysis**

I. Introduction

Recently, successful implementations of mutually injection-locked oscillators through inductor coupling have been demonstrated [1]-[14]. In a two-oscillator system, the tuning range versus a tuning parameter is increased due to the two resonance frequencies exhibited by the coupled resonators [7]-[9]. Other applications include sensors [4], [10]-[13] and near-field wireless data systems in the vein of [14] at 13.35 MHz and 30 MHz. In addition, the oscillator coupling enables a reduction of phase-noise, which follows the rule $S_N = S - 10\log_{10}N$ [15] where S is the spectral density of a single oscillator [16] and N is the number of oscillator elements.

Despite the interest in inductively coupled oscillators, there is a lack of insightful analysis tools for these configurations, in which several oscillation modes may coexist. The work [3] proposes a useful eigenvector/eigenvalue analysis [17]-[19] of the full oscillator system, which takes advantage of the circulant structure of the coupling matrix. The coexistent oscillation modes are identified; however, the analysis described is not valid in the presence of asymmetries. In turn, the recent work [20] presents an investigation of two mutually injection-locked oscillators that is not restricted to identical oscillators. However, the analysis relies on a linearization of the total admittance functions of the individual oscillators about their standalone free-running solutions [21]-[26], which limits its accuracy to weak coupling conditions [27]-[28].

As shown in this work, nonlinear effects can be observed from rather small values of the inductive coupling factor k. To account for these effects, we will extend [20] by addressing the coupled system under significant deviations of the oscillator elements with respect to their free-running solutions. Initially, an analytical formulation is derived, which provides insight into the qualitative transformations undergone by the system when increasing the mutual coupling. Each oscillator is affected by the other, so the behavior is more complex than in oscillators injection locked by an independent source [29]-[30]. As will be demonstrated, families of disconnected curves that merge from a certain k value are obtained versus a tuning parameter.

To analyze a realistic system of transistor-based coupled oscillators, one must keep in mind the coexistence of solutions revealed by the analytical investigation. In fact, unveiling the behavior pattern of inductively coupled oscillators is the main contribution of this work. The use of time-domain integration would require a global exploration of all the possible initial values (which is virtually impossible) since each stable solution has its own basin of attraction [31]-[32]. The problem would be similar in the envelope domain [33]-[35]. On the other hand, when using harmonic balance (HB) one must be able to lead each oscillator to an oscillatory state, which can be done connecting an auxiliary generator (AGs) to each oscillator element [29]-[36]. The amplitude of each AG, together with their phase shift and the oscillation frequency, must be optimized to fulfill (simultaneously) the oscillation condition at the two oscillator elements. However, this procedure often fails due to the need to fulfill four goals, corresponding to the zero value of the real and imaginary part of the admittance function in each oscillator [18], [29], using only two observation/analysis nodes. Here an alternative numerical method will be presented. The oscillators are described with

This work was supported in part by the Spanish Ministry of Economy and Competitiveness and the European Regional Development Fund (ERDF/FEDER) under research project TEC2017-88242-C3-1-R.

This paper is an expanded version from the IEEE MTT-S International Microwave Symposium (IMS 2020).

A. Suárez and F. Ramírez are with the Communications Engineering Department, University of Cantabria, 39005, Santander, Spain (e-mail: suareza@unican.es; ramirezf@unican.es).

R. Melville is with is with EMECON, LLC, Berkeley Heights, NJ, USA, (e-mail: robert.melville@ieee.org).

numerical nonlinear admittance functions, extracted from HB, while the passive coupling network is described with a linear admittance matrix. Advantage is taken of the fact that the oscillator admittance functions do not depend on the excitation phase. Instead, the phase shift between the oscillator elements is considered in the formulation of the entire system, which is solved separately from HB, using custom software. The methodology constitutes the first generalization of the semi-analytical formulation of coupled-oscillator systems [21]-[22] to oscillators described with nonlinear admittance functions. Furthermore, judicious mathematical conditions allow extending the contour-intersection technique in [37]-[38] to the coupled system. This procedure (which is not based on continuation [39]-[41]) allows the simultaneous and exhaustive detection of all the oscillation modes coexisting for a given parameter value.

The paper is organized as follows. Section II summarizes the linearized analysis of two inductively coupled injection-locked oscillators at the ratio 1:1 presented in [20]. Section III describes the nonlinear analytical investigation of this system. Section IV presents the numerical analysis method, applicable to realistic transistor-based oscillators. Section VI describes the extension of this method to the oscillator coupling at the ratio 1:*N*.

II. Two Mutually Injection-Locked Oscillators at 1:1 with Linear Oscillator Models

A. System description

Let a general system of two inductively coupled oscillators at the frequency ratio 1:1 be considered. The system is shown in Fig. 1(a). The passive-linear coupling network (in dashed line) will be described with its admittance matrix:

$$\begin{bmatrix} y_{11} & y_{12} \\ y_{21} & y_{22} \end{bmatrix} = \begin{bmatrix} \dfrac{-jL_2}{\left(-M^2+L_1L_2\right)\omega} & \dfrac{jM}{\left(-M^2+L_1L_2\right)\omega} \\ \dfrac{jM}{\left(-M^2+L_1L_2\right)\omega} & \dfrac{-jL_1}{\left(-M^2+L_1L_2\right)\omega} \end{bmatrix} \quad (1)$$

where L_1 and L_2 are the inductors of the first and second oscillator and $M = k\cdot(L_1L_2)^{1/2}$ is the coupling inductance. Note that, in the general case, the admittance matrix y_{ij} may include parasitics. The oscillators are described by their individual admittance functions $Y_{T1}(V,\omega)$ and $Y_{T2}(V,\omega)$, where V and ω are the amplitude and frequency of the excitation voltage. Assuming mutually injection-locked operation at the frequency ω, the coupled system can be described (at the fundamental frequency) with the complex system:

$$\begin{aligned} &\left[Y_{T1}(V_1,\omega)+j/(L_1\omega)+y_{11}(\omega)\right]V_1+y_{12}(\omega)V_2e^{j\phi}=0 \\ &\left[Y_{T2}(V_2,\omega)+j/(L_2\omega)+y_{22}(\omega)\right]V_2e^{j\phi}+y_{12}(\omega)V_1=0 \end{aligned} \quad (2)$$

where V_1 and V_2 are the oscillation amplitudes and ϕ is the phase shift between the two voltage signals. Note that the admittance $-j/(L_i\omega)$ associated with the coupled inductor in each oscillator has to be subtracted from the functions Y_{T1} and Y_{T2} since this inductive effect is included in (1).

Several previous works [19]-[26] have successfully developed semi-analytical formulations of complex systems based on admittance-type oscillator models extracted from HB simulations. However, in all these works the admittance-type models are linearized about their corresponding standalone free-running solutions, which is valid under the assumption of a small deviation from these solutions once each oscillator is introduced into the system. In the case of (2), the two admittance functions $Y_{T1}(V_1,\omega)$ and $Y_{T2}(V_2,\omega)$ are linearized [20] about their respective free-running solutions, which, as will be shown, limits the validity of the analysis to small k values. Here we will address for the first time the nonlinear operation of the inductively coupled system, considering the two bi-variable nonlinear functions $Y_{T1}(V_1,\omega)$ and $Y_{T2}(V_2,\omega)$, instead of their linearized approximations. To facilitate the comparison between the linear and nonlinear cases, the next sub-section summarizes the results obtained in [14], with linearized oscillator models.

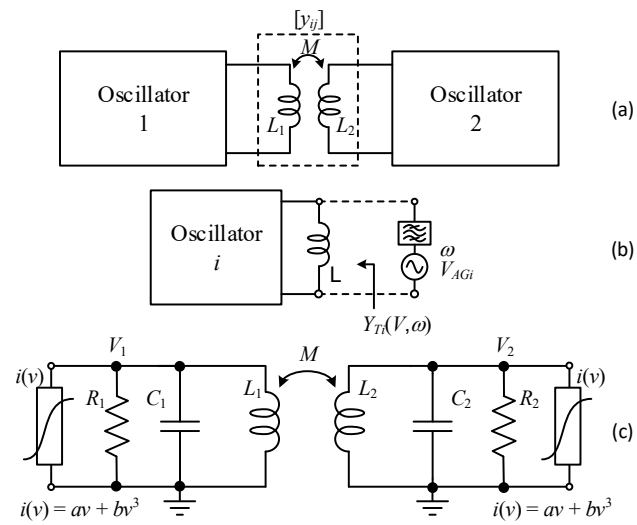

Fig. 1. Inductively coupled oscillators. (a) General system. (b) Extraction of the individual oscillator models with the aid of an AG. Finite differences are applied to linearize each oscillator admittance function about its free-running solution. (c) Simple circuit used for the validation of the analytical expressions in Section II and III through comparison with HB simulations. The element values a = -0.03 A/V, b = 0.01 A/V^3, $L_{1,2} = L$ = 33 nH, C_2 = 76.7 pF, $R_{1,2} = R$ = 100 Ω.

B. Formulation based on linearized models

The system based on linearized oscillator models (valid for small k) will allow obtaining the variation of the coupled-system solution versus a parameter η (a capacitor value, for instance). The frequency and amplitude of the free-running solution (in standalone operation) of each of the two distinct oscillators are given by ω_{oi} and V_{oi}, where i = 1,2. In practice, these free-running solutions can be calculated with the aid of an AG [Fig. 1(b)], optimizing its amplitude V_{AG} and frequency ω_{AG} to obtain a zero value of the AG current-to-voltage: Y_{AGi}, where i = 1, 2 [18], [29]. In fact, the AG admittance function agrees with the defined oscillator-admittance function $Y_{Ti}(V_i,\omega)$. In the linearized analysis, this function is described with its first-order Taylor series expansion about the free-running solution fulfilling $Y_{Ti}(V_{oi},\omega_{oi}) = 0$. The amplitude derivative $\partial Y_{Ti} / \partial V_i$ is calculated by setting the AG frequency to $\omega_{AG} = \omega_{oi}$ and

considering a small increment in the voltage amplitude V_{AG} about V_{oi} [17]. Note that a full HB analysis, with as many harmonic components as desired, is carried out after the application of the increment in V_{AG}. Likewise, the frequency derivative $\partial Y_{Ti} / \partial \omega$ is calculated by setting the AG amplitude to $V_{AG} = V_{oi}$ and considering a small increment in the AG frequency about ω_{oi} [23]-[24]. Finally, the derivative $\partial Y_{Ti} / \partial \eta$ will be obtained through the same procedure: considering a small increment in η about the free-running point V_{oi}, ω_{oi}.

Synchronized operation of the inductively coupled oscillator system at the frequency ω will be assumed. Under a small variation of the parameter η, it will be approximately described as follows:

$$\begin{bmatrix} \frac{\partial Y_{T1}}{\partial V_1}(V_1 - V_{1o}) + \frac{\partial Y_{T1}'}{\partial \omega}(\omega - \omega_o) + \\ \frac{\partial Y_{T1}}{\partial \eta}(\eta - \eta_o) + j\frac{1}{L_1 \omega_o} + y_{11}(\omega_o) \end{bmatrix} V_1 + \left[y_{12}(\omega_o) + \frac{\partial y_{12}}{\partial \omega}(\omega - \omega_o) \right] V_2 e^{j\phi} = 0 \quad (3)$$

$$\left[\frac{\partial Y_{T2}}{\partial V_2}(V_2 - V_{2o}) + \frac{\partial Y_{T2}'}{\partial \omega}(\omega - \omega_o) + j\frac{1}{L_2 \omega_o} + y_{22}(\omega_o) \right] V_2 e^{j\phi} + \left[y_{12}(\omega_o) + \frac{\partial y_{12}}{\partial \omega}(\omega - \omega_o) \right] V_1 = 0$$

where for simplicity the two oscillators are assumed to have the same free-running frequency $\omega_{o1} = \omega_{o2}$. In addition, the following quantities (evaluated at ω_o) have been defined:

$$\frac{\partial Y_{T1}'}{\partial \omega} = \frac{\partial Y_{T1}}{\partial \omega} - j\frac{1}{L_1 \omega^2} + \frac{\partial y_{11}}{\partial \omega}, \quad \frac{\partial Y_{T2}'}{\partial \omega} = \frac{\partial Y_{T2}}{\partial \omega} - j\frac{1}{L_2 \omega^2} + \frac{\partial y_{22}}{\partial \omega} \quad (4)$$

To obtain the solution, (3) is split into real and imaginary parts, which provides a system of four real equations in four unknowns: V_1, V_2, ϕ, ω. In practice, the system is solved by sweeping ϕ, and solving for V_1, V_2, ω and η.

The above analysis has been applied to two oscillators of the Van der Pol type [shown in Fig. 1(c)], with the element values a = -0.03 A/V, b = 0.01 A/V^3, $L_1 = L_2$ = 33 nH, C_2 = 76.7 pF, $R_1 = R_2$ = 100 Ω. The two oscillators are assumed identical, except for $C_1 = C_2 + \Delta C_1$, acting like the analysis parameter $\eta = C_1$. System (3) only enables a valid prediction of the steady-state solutions for very small k values. In the analysis of Fig. 2(a), the coupling factor is set to $k = 0.01$. In that figure, the phase ϕ has been represented versus ΔC_1. The results of the analytical formulation are compared with a HB simulation with 15 harmonics (connecting an AG to each oscillator). The excellent agreement is because the derivatives of Y_{T1} and Y_{T2} are calculated with the HB system as an inner tier [26], considering the same number of harmonic terms. As will be shown in the next section, under a coupling factor as small as $k = 0.1$, the coupled system exhibits a nonlinear behavior that prevents the linearization of the oscillator admittance functions about the individual free-running oscillations.

The stability and phase-noise analyses are based on the introduction of a small perturbation of complex frequency in system (3), which involves a subsequent linearization with respect to each solution obtained versus ΔC_1, as shown in the previous work [19]. Fig. 2(b) presents the variation of the real part of the dominant poles versus the phase shift ϕ of the steady-state solution. A real pole crosses through zero at each turning point of the solution curve, which is stable between the ϕ values 90º and -90º. Fig. 2(c) presents the variation of the phase-noise at 1 kHz offset from the carrier versus the phase shift ϕ. This phase noise is compared with the one obtained in free-running conditions, represented in dotted line. For this small coupling factor, a phase noise reduction of 3 dB is obtained in small phase-shift intervals about 0º and 180º.

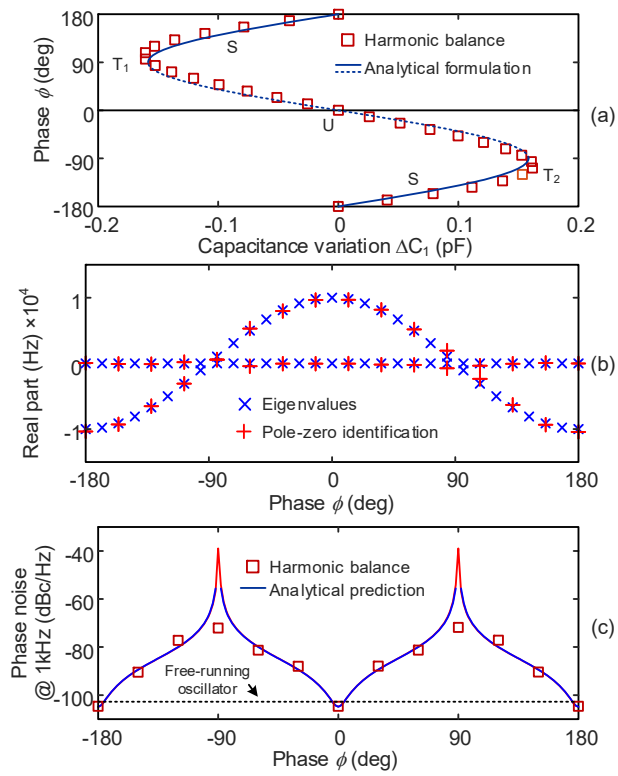

Fig. 2. Validation of the analysis method through comparison with circuit-level HB simulations. (a) Phase shift ϕ versus ΔC_1. (b) Real part of the dominant poles versus ϕ. The stable interval is comprised between 90º and -90º. (c) Phase-noise spectral density at 1 kHz offset versus ϕ. It is compared with the free-running value, in dotted line.

III. Nonlinear Analytical Formulation of Two Mutually Injection-Locked Oscillators

The inductive coupling factor can take any value $0 < k < 1$, so in most cases it will not be possible to linearize the admittance functions $Y_{T1}(V,\omega)$ and $Y_{T2}(V,\omega)$ of the two individual oscillators about their respective free-running solutions. In the following derivations, this linearization is avoided, and the oscillators are described with nonlinear admittance models.

A. Formulation

The nonlinear behavior of the two inductively-coupled oscillators can be understood by particularizing (2) to the system of two van der Pol oscillators in Fig. 1(c). The cubic nonlinearity in each oscillator is modeled with its corresponding describing function limited to the fundamental frequency, which provides the following matrix system:

$$\begin{bmatrix} G_T + \frac{3}{4}bV_1^2 + jF_1(\omega) & \frac{jk}{\left(-k^2+1\right)L\omega} \\ \frac{jk}{\left(-k^2+1\right)L\omega} & G_T + \frac{3}{4}bV_2^2 + jF_2(\omega) \end{bmatrix} \begin{bmatrix} V_1 \\ V_2 e^{j\phi} \end{bmatrix} = 0 \quad (5)$$

where $L_{1,2} = L$, $R_{1,2} = R$, $G_T = a + 1/R$ and, for compactness, the following definitions have been introduced:

$$F_1(\omega) = C_1\omega - \frac{1}{\left(-k^2+1\right)L\omega}$$
$$F_2(\omega) = C_2\omega - \frac{1}{\left(-k^2+1\right)L\omega} \quad (6)$$

The complex system (5) contains four unknowns V_1, V_2, ω, ϕ. The initial objective is to eliminate the phase shift ϕ, and derive a system of three real equations in the remaining three unknowns V_1, V_2, ω. It is taken into account that (5) is homogeneous, so its associated matrix must be singular, which provides:

$$\det\begin{bmatrix} G_T + \frac{3}{4}bV_1^2 + jF_1(\omega) & \frac{jk}{\left(-k^2+1\right)L\omega} \\ \frac{jk}{\left(-k^2+1\right)L\omega} & G_T + \frac{3}{4}bV_2^2 + jF_2(\omega) \end{bmatrix} = \quad (7)$$
$$\left[G_T + \frac{3}{4}bV_1^2 + jF_1(\omega)\right]\left[G_T + \frac{3}{4}bV_2^2 + jF_2(\omega)\right] + P(\omega) = 0$$

where the following additional definition has been used:

$$P(\omega) = \frac{k^2}{\left(-k^2+1\right)^2 (L\omega)^2}$$

From the first row of (5), one can derive the complex equation:

$$\left(G_T + \frac{3}{4}bV_1^2 + jF_1(\omega)\right)V_1 = -\frac{jk}{\left(-k^2+1\right)L\omega}V_2 e^{j\phi} \quad (8)$$

Now, splitting the complex equation (7) into real and imaginary parts and obtaining the squared magnitude of (8), one obtains the following system of three real equations in the three real unknowns V_1, V_2 and ω:

$$\left(G_T + \frac{3}{4}bV_1^2\right)\left(G_T + \frac{3}{4}bV_2^2\right) - F_1(\omega)F_2(\omega) + P(\omega) = 0 \quad \text{(a)}$$
$$\left(G_T + \frac{3}{4}bV_2^2\right)F_1(\omega) + \left(G_T + \frac{3}{4}bV_1^2\right)F_2(\omega) = 0 \quad \text{(b) (9)}$$
$$\left[\left(G_T + \frac{3}{4}bV_1^2\right)^2 + F_1^2(\omega)\right]V_1^2 = P(\omega)V_2^2 \quad \text{(c)}$$

In the above system, one can make the amplitudes V_1 and V_2 disappear and, thus, obtain a real equation in the frequency ω:

$$H_\pm = F_2(\omega)\left(\begin{matrix} F_1^2(\omega)G_T + \\ F_2(\omega)\left(\begin{matrix} \pm\sqrt{-F_2^2(\omega)F_1^2(\omega) + P(\omega)F_1(\omega)F_2(\omega)} - \\ F_1(\omega)G_T \end{matrix}\right) \end{matrix}\right)^2 -$$
$$F_1^4(\omega)\left(-F_1^2(\omega)F_2(\omega) + P(\omega)F_1(\omega)\right) = 0 \quad (10)$$

The above equation cannot be solved explicitly but provides the two error functions (H_+ and H_-), respectively corresponding to the plus and minus signs before the square root. The zeroes of (10) provide the frequencies of the potential solutions. Note that additional conditions on V_1 and V_2 must be fulfilled. The error functions $H_\pm$ obtained for $C_1 = 77$ pF and several values of the coupling factor k are shown in Fig. 3. For each k, the frequency values of the potential solutions correspond to the crossings through zero.

Once the potential-solution frequencies are known, one can apply a straightforward procedure to obtain the solution amplitudes. Using (9)(a) and (9)(b), one derives the following directly solvable equations:

$$\left(G_T + \frac{3}{4}bV_1^2\right)^2 = -F_1^2(\omega) + P(\omega)\frac{F_1(\omega)}{F_2(\omega)}$$
$$G_T + \frac{3}{4}bV_2^2 = -\left(G_T + \frac{3}{4}bV_1^2\right)\frac{F_2(\omega)}{F_1(\omega)} \quad (11)$$

On the other hand, actual solutions must also fulfill (9)(c):

$$\left[\left(G_T + \frac{3}{4}bV_1^2\right)^2 + F_1^2(\omega)\right]V_1^2 = P(\omega)V_2^2 \quad (12)$$

Once the amplitudes V_1 and V_2 are known, the phase shift between the two elements is obtained from (8).

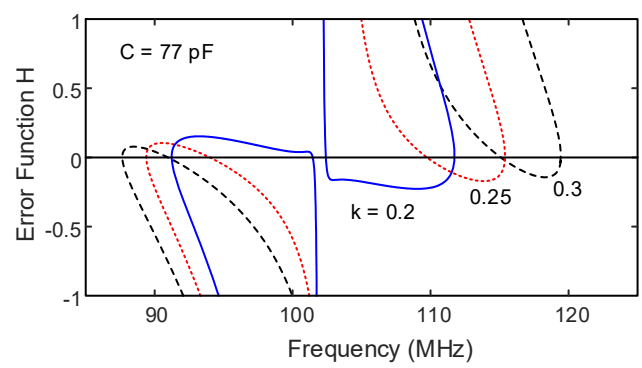

Fig. 3. Analytical study. Error functions for the frequency calculation when considering three different values of the coupling factor k.

In case the two oscillators are identical, $\Delta C = 0$, one obtains the two in-phase (0º) and out-of-phase (180º) modes with the identical amplitudes $V_1 = V_2$ resulting from the eigenvalue analysis in [3] and [17]. However, as will be shown here, and for relatively low values of the coupling factor k, there will also be two other modes with different amplitudes ($V_1 \neq V_2$) in the two oscillators. The frequency of the non-symmetric modes is determined by the condition:

$$F_1(\omega) = F_2(\omega) = 0 \quad (13)$$

which provides a particular null of the error function (10). From (13), the frequency of the non-symmetric solutions is:

$$\omega = \sqrt{\frac{1}{\left(1-k^2\right)LC}} \tag{14}$$

The phase shift values can be obtained from the first equation in (5):

$$\left(G_T + \frac{3}{4}bV_1^2\right)V_1 + jT(\omega)V_2 e^{j\phi} = 0, \quad T(\omega) = \frac{k}{\left(1-k^2\right)L\omega} \tag{15}$$

where (13) has been taken into account. Because the amplitudes V_1 and V_2 are positive and different, there can only be two possible values of phase shift, given by $\phi = \pm\pi/2$. Thus, the amplitudes of the remaining solutions fulfill:

$$\begin{aligned} &\left(G_T + \frac{3}{4}bV_2^2\right)V_2 = \mp T(\omega)V_1 \quad \text{(a)} \\ &\left(G_T + \frac{3}{4}bV_1^2\right)V_1 = \pm T(\omega)V_2 \quad \text{(b)} \end{aligned} \tag{16}$$

where the upper (lower) signs in (a) and (b) are associated and correspond to a same solution. Note that the relationships (16) can also be derived from (12). These non-symmetrical solutions under identical oscillators are obtained here for the first time to our knowledge.

B. Behavior when increasing the coupling factor k

Using the above procedure, we have obtained the solution curves of the two inductively coupled Van der Pol oscillators versus the capacitance C_1 (in the first oscillator) when increasing k. The potential-solution frequencies are calculated performing a double sweep in C_1 and ω, and obtaining the zero-value contours of $H_\pm$. Then, the solution curves are achieved using the additional equations (11) and (12). When considering different values of the coupling factor $k = 0.1$, 0.12 and 0.2, one obtains the evolution shown in Fig. 4 ($k = 0.1$), Fig. 5 ($k = 0.15$) and Fig. 6 ($k = 0.2$). In each case, the oscillation frequency, amplitudes and phase shift are represented in (a), (b) and (c), respectively, versus C_1. For validation, the results are compared with circuit-level HB simulations using two AGs. However, one must note the following: (i) The HB convergence is facilitated by the simple topology of the cubic-nonlinearity oscillators. (ii) The HB solution curves could only be obtained by first providing the values resulting from the analytical formulation to the AGs used in this HB simulation. The AG optimization confirmed the validity of these analytical solutions. Then the solution curves could be completed in HB due to the inherent continuation procedure of the HB sweep.

For the lower k values (Fig. 4), one obtains three disconnected solution curves. One is a closed eight-shaped curve, whereas the other two curves are open. Note that in the amplitude representation of Fig. 4(a) there are actually two curves for each solution, since the amplitudes are different in the two oscillators. In the closed solution curve of Fig. 4(a), containing an expanded view, the amplitudes of the two oscillators have high values. They are both in an oscillatory state and mutually injection locked. On the other hand, in each of the two open curves, one of the two oscillators is dominant (a different one in each solution), and the other one responds to the coupled signal. This is evidenced by the difference in the amplitude values [Fig. 4(a)]. In one of the open solutions [extending from 60 pF to 95 pF in the representation of Fig. 4(a)], the higher amplitude is V_1 (in the order of 1.7 V) and the lower one is V_2 (below 0.5 V). In the other open solution, the situation is opposite.

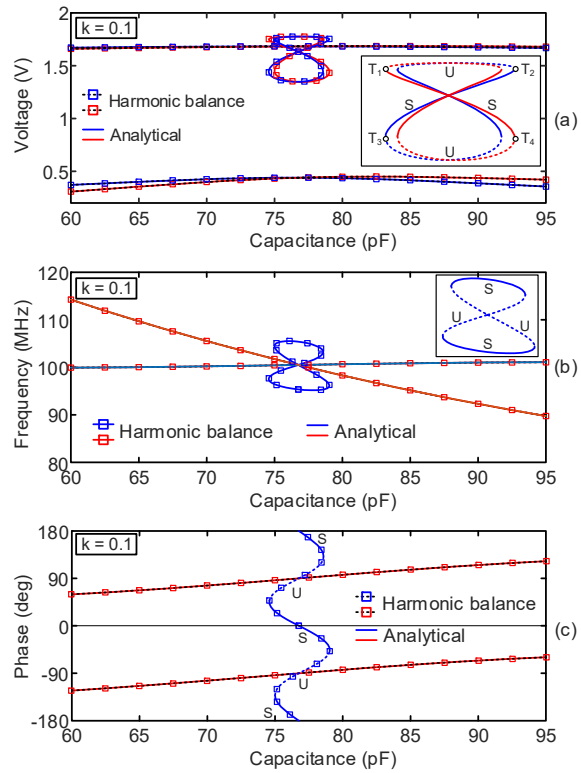

Fig. 4. Analytical study. Coupling factor $k = 0.1$. Analytical results are compared with HB simulations. (a) Frequency variation versus C_1. (b) Amplitude variation. (c) Variation of the phase shift.

As gathered from Fig. 4(b), for each C_1, there are three solution frequencies. This is can be seen at $\Delta C = 0$, where two of these frequencies agree with those of the two in-phase and out-of-phase modes $\omega = 1/\sqrt{LC(1\pm k)}$ (for which the amplitudes of the two oscillators are equal $V_1 = V_2$) [20], and the third frequency is $\omega = 1/\sqrt{LC(1-k^2)}$ (for which $V_1 \neq V_2$). Regarding the phase shift, and in agreement with (13) to (16), for two identical oscillators ($\Delta C = 0$), besides the two modes with phase shifts 0º and 180º, there are two other modes with the phase shifts ± 90º, the same frequency $\omega = 1/\sqrt{LC(1-k^2)}$ and distinct amplitudes .

When increasing k, the closed eight-shaped curve splits into two sections and each section merges with one of the open curves [Fig. 6], to give rise to two distinct open solution curves. In these open curves, each oscillator is dominant at each side of the middle value $\Delta C = 0$. The described curve merging can be compared with the structural behavior of a single oscillator injection locked by an independent source [29]-[30], [42]-[43]. In that case, when increasing the amplitude of the injection source, a single closed curve and a single open curve merge into a unique curve, which for the lower values of the input amplitude exhibits turning points or folding. Here, when

increasing k, we obtain a double family of curves, one corresponding to each operation mode. In one of the two modes V_1 is higher (lower) than V_2 for $\Delta C < 0$ ($\Delta C > 0$). The opposite is true of the other mode. The curves exhibit turning points for intermediate k values (Fig. 5), at which the HB simulations undergo a discontinuous jump. The curves become less intricate when increasing k, as gathered from Fig. 5 and Fig. 6.

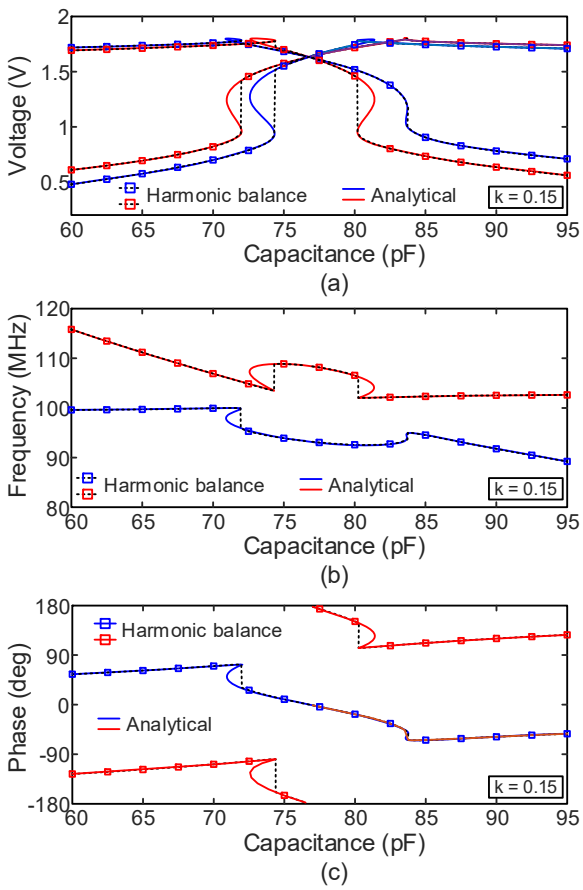

Fig. 5. Analytical study. Coupling factor $k = 0.15$. Analytical results are compared with HB simulations. (a) Frequency variation versus C_1. (b) Amplitude variation. (c) Variation of the phase shift.

The variation of the phase shift versus the analysis parameter C_1 is shown in Fig. 4(c), 5(c) and 6(c). As stated, for the lower k values and $\Delta C = 0$ there are always two modes with the respective phase shifts 0º and 180º, as well as two additional modes with ± 90º. In the closed solution curves versus C_1, the phase variations are strong and cover the whole range -180º to 180º. When increasing k the closed curves split and merge, and the modes with ± 90º at $\Delta C = 0$ disappear [Fig. 5(c)]. In the open curves, the phase excursion decreases with k. Thus, for sensor applications, one should use a relatively small k.

To understand the stability properties of the coexisting modes, one should note that the eight-shaped solution curves obtained for the lower k values exhibit 4 turning points (T_1, T_2, T_3, T_4), as seen in Fig. 4. At each turning point a real pole crosses through zero. Performing a stability analysis, one obtains that the section of the eight-shaped curve comprised between T_1 and T_4 is stable, and so is the section between T_2 and T_3. Thus, there are two coexistent stable modes. at the turning points, the oscillators become unlocked and there is a transition to a doubly autonomous quasi-periodic regime. On the other hand, the open solution curves are always unstable.

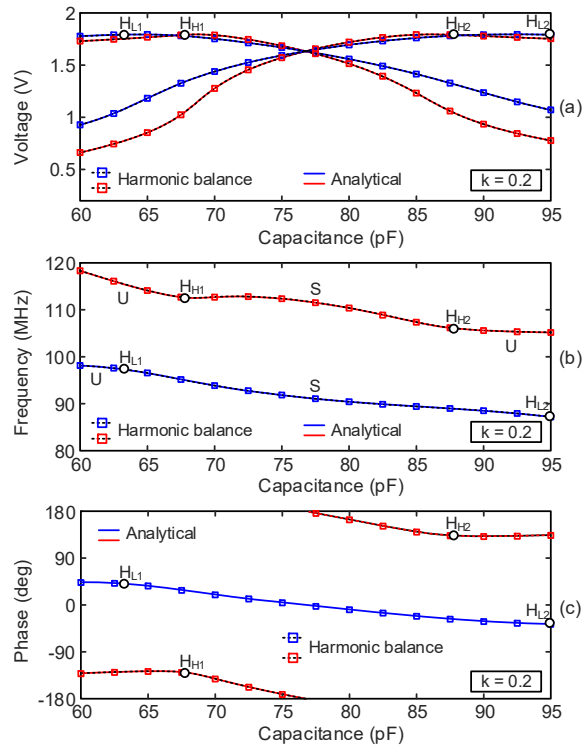

Fig. 6. Analytical study. Coupling factor $k = 0.2$. Analytical results are compared with HB simulations. Hopf bifurcations are indicated. (a) Frequency variation versus C_1. (b) Amplitude variation. (c) Variation of the phase shift.

After each eight-shaped curve splits and merges with one of the open solution curves, Hopf bifurcations will take place (from certain k) in the two single and distinct open curves. This is illustrated in Fig. 7(a), which presents the stability analysis of the two independent oscillation modes obtained for $k = 0.2$ using pole-zero identification [44]-[46]. The real part of the dominant poles has been represented versus C_1. The two modes are stable in the central interval about $\Delta C = 0$. This stable interval is bounded by secondary Hopf bifurcations [Fig. 7(a)] at which a pair of complex-conjugate poles crosses the imaginary axis to the right-hand side of the complex plane [29], [42], [47]. When the Hopf bifurcation occurs, the system evolves into a self-oscillating mixer regime. The detected Hopf bifurcations have been superimposed in Fig. 6. The length of the stable intervals is different for the two modes. When the two modes are simultaneously stable, one or another will be experimentally observed depending on the initial conditions. This has been validated with the time-domain simulations in Fig. 7(b) and (c). Note that the coexistence of stable periodic modes with different phase shift is possible due to presence of unstable DC and quasi-periodic solutions [48]-[49], acting as separators of the basins of attraction of the two coexistent stable modes.

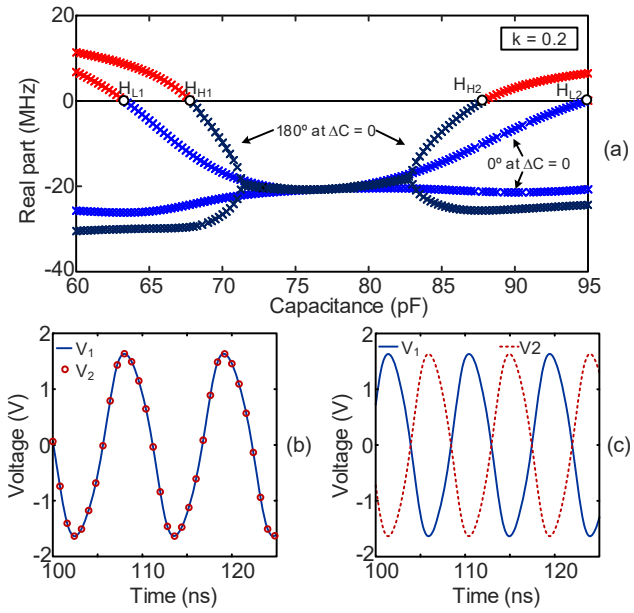

Fig. 7. Stability analysis using pole-zero identification of the two independent oscillation modes obtained for $k = 0.2$. Validation with time-domain simulations. (a) Pole-zero identification. The secondary Hopf bifurcations of each mode are indicated. (b) and (c) Time-domain simulations. Steady-state waveforms in the two oscillators obtained for two different initial conditions at $\Delta C = 0$, with 0º and 180º phase shift, respectively.

To summarize, under small k values, there is a closed solution curve through which the two oscillators are in an oscillatory state and mutually injection locked, plus two other disconnected curves in which system behaves as if only the first (second) oscillator is in an oscillatory state and the second (first) oscillator is responding to this oscillation signal. From certain k, two distinct parts of the previously closed curve merge separately with the disconnected curves and give rise to two open curves at different frequencies, each corresponding to a different oscillation mode. After this merging, the two open curves exhibit strong folding due to the presence of turning points, or infinite-slope points. The higher phase sensitivity is obtained for the smaller k values, through the closed solution curves.

IV. Nonlinear Numerical Analysis of Two Mutually Injection-Locked Oscillators

In this section, a general numerical analysis of two inductively coupled transistor-based oscillators will be presented. As explained below, for this numerical analysis the coupled system is best formulated in the following manner:

$$\left\{\begin{bmatrix} Y_{A1}(V_1,\omega) & 0 \\ 0 & Y_{A2}(V_2,\omega) \end{bmatrix} + \begin{bmatrix} y_{p11}(\omega,k,\eta) & y_{p12}(\omega,k,\eta) \\ y_{p21}(\omega,k,\eta) & y_{p22}(\omega,k,\eta) \end{bmatrix}\right\} \begin{bmatrix} V_1 \\ V_2 e^{j\phi} \end{bmatrix} = 0 \qquad (17)$$

where the nonlinear-admittance functions $Y_{A1}(V_1,\omega)$ and $Y_{A2}(V_2,\omega)$ may not strictly correspond to the standalone oscillator circuits; they may represent just part of these oscillators. In that case, the passive admittance matrix $\left[y_p(\omega,k,\eta)\right]$ accounting, in principle, for the coupling network (and depending on the coupling factor k), would also include part of the linear networks of these oscillators. For convenience, the analysis parameter η (a tuning capacitor, for instance) might be also be included in $\left[y_p(\omega,k,\eta)\right]$. The subtraction of the linear elements to be included in the coupling network is performed after the calculation of those functions (with the aid of auxiliary generators).

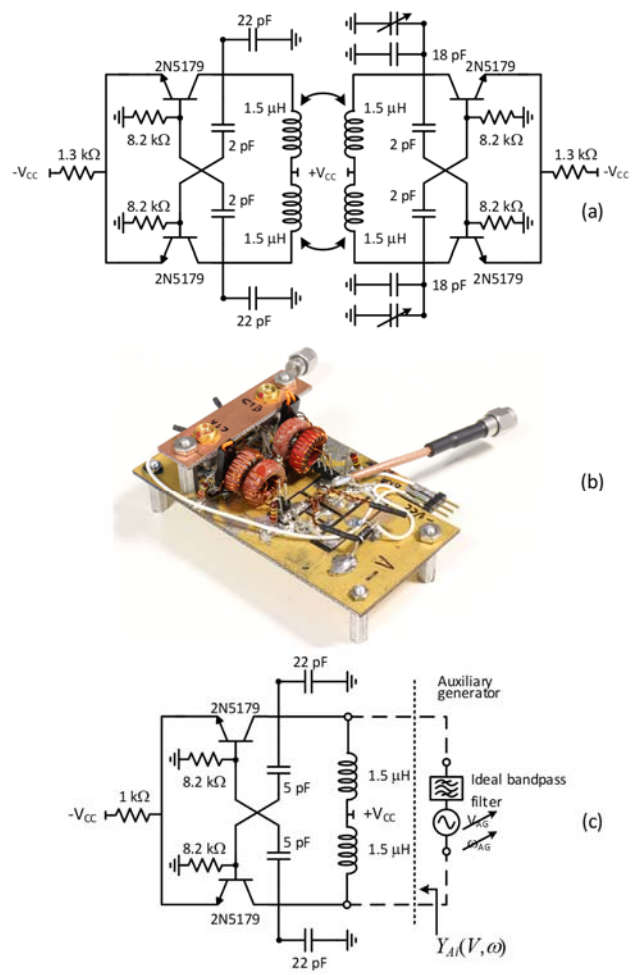

Fig. 8. Coupled system using differential bipolar-based oscillators. (a) Schematic. (b) Photograph. (c) Sketch indicating the procedure to extract the admittance functions $Y_{A1}(V_1,\omega)$ and $Y_{A2}(V_2,\omega)$ of the individual oscillators.

The procedure will be illustrated through its application to the system of two differential bipolar-based oscillators shown in Fig. 8(a)-(b). When uncoupled, they oscillate at the frequency $f_o = 25$ MHz (for $C_1 = C_2 = 22$ pF). To obtain each function $Y_{Ai}(V,\omega)$, where $i = 1,2$, each oscillator is simulated with an AG connected between the terminals at which this admittance function is defined, as shown in Fig. 8(c). Then a double sweep in ω and V is carried out. The flexibility in the choice of the analysis terminals, as well as the order of the nested sweeps (with the one in V being the internal one), should avoid potential convergence problems of HB. In principle, system (17) could be solved through a Newton iteration, after a

suitable analytical modelling of the nonlinear active admittance functions, though this is beyond the scope of this initial paper. On the other hand, the advantage of the procedure presented in the following is that it enables an exhaustive search of solution curves and operation modes, which would not be possible through an ordinary error-minimization/continuation method [39]-[41].

To solve (17), advantage is taken of the fact that each of the admittance functions $Y_{A1}(V_1,\omega)$ and $Y_{A2}(V_2,\omega)$ depends only on the amplitude and frequency of its own excitation. The singular determinant associated with the autonomous system (17) is:

$$\det\begin{bmatrix} Y_{A1}(V_1,\omega)+y_{p11}(\omega,k,\eta) & y_{p12}(\omega,k,\eta) \\ y_{p21}(\omega,k,\eta) & Y_{A2}(V_2,\omega)+y_{p22}(\omega,k,\eta) \end{bmatrix} = \left(Y_{A1}+y_{p11}\right)\left(Y_{A2}+y_{p22}\right)-y_{p12}y_{p21}=0 \tag{18}$$

The advantage of the above equation is that it does not depend on the phase shift. Thus, for each pair of values k,η, (18)can be compactly re-written as:

$$\det(V_1,V_2,\omega)=0 \tag{19}$$

Solving (17) for $e^{j\phi}$ in terms of V_1 and V_2, one obtains:

$$e^{j\phi}=-\frac{(Y_{A1}+y_{p11})V_1}{y_{p12}V_2} \tag{20}$$

And setting the magnitude of the expression in (20) to 1 one obtains the following system of three equations in three unknowns V_1,V_2,ω:

$$\begin{aligned} &\det{}^r(V_1,V_2,\omega)=0 && \text{(a)} \\ &\det{}^i(V_1,V_2,\omega)=0 && \text{(b)} \\ &H=\left|\frac{\left[Y_{A1}(V_1,\omega)+y_{p11}(\omega)\right]V_1}{y_{p12}(\omega)V_2}\right|=1 && \text{(c)} \end{aligned} \tag{21}$$

where the superscripts r and i indicate real and imaginary parts. The practical solution of (21) is carried out in two stages. In a first stage, for each pair of values η, ω, one obtains two surfaces $S_1=\left\{V_1,V_2,\det{}^r(V_1,V_2)\right\}$ and $S_2=\left\{V_1,V_2,\det{}^i(V_1,V_2)\right\}$. Then, one should calculate the intersection of the surface S_1 with the plane of zero value $\det{}^r=0$, and the intersection of the surface S_2 with the plane of zero value $\det{}^i=0$. For each η, ω, these intersections provide two curves $C^r(V_1,V_2)$ and $C^i(V_1,V_2)$ in the plane defined by V_1 and V_2. Then, the potential solution points of (19) at the particular values η, ω are given by the intersections between the two curves C^r and C^i:

$$P_{\eta,\omega}(V_1,V_2)=C^r(V_1,V_2)\cap C^i(V_1,V_2) \tag{22}$$

where P stands for point. For each η and sweeping ω, $P_{\eta,\omega}(V_1,V_2)$ gives rise to one or more curves in the plane defined by V_1 and V_2, denoted as: $D_\eta(V_1,V_2)$, where D refers to "determinant". However, equation (21)(c) must also be fulfilled.

As an example, Fig. 9(a) presents the curves $D_\eta(V_1,V_2)$, composed by the points at which $\det(V_1,V_2,\omega)=0$ obtained for the coupling factor k = 0.21 and the capacitor value C_2 = 21 pF, which have been traced in blue. Note that all the points in the blue curves of Fig. 9(a) fulfill both $\det^r=0$ and $\det^i=0$. As stated, the actual solution points should also satisfy H = 1 [in (21)(c)]. For convenience, two functions are considered, respectively obtained by solving for $e^{j\phi}$ from each of the two complex equation composing the matrix system (17). These independent solutions are:

$$e^{j\phi}=-\frac{(Y_{A1}+y_{p11})V_1}{y_{p12}V_2}=-\frac{y_{p21}V_1}{(Y_{A2}+y_{p22})V_2} \tag{23}$$

Note that when (18) is fulfilled, the two equations are identical. For each pair of values η, ω, by setting the magnitude of each of the two expressions in (23) to 1, one obtains one or more curves in the plane V_1, V_2. These curves are defined by:

$$\begin{aligned} H_1(V_1,V_2)&=\left\{V_1,V_2 \,\middle|\, abs\left(\frac{(Y_{A1}+y_{p11})V_1}{y_{p12}V_2}\right)=1\right\} \\ H_2(V_1,V_2)&=\left\{V_1,V_2 \,\middle|\, abs\left(\frac{y_{p21}V_1}{(Y_{A2}+y_{p22})V_2}\right)=1\right\} \end{aligned} \tag{24}$$

When sweeping ω, the intersections of $H_1(V_1,V_2)$ and $H_2(V_1,V_2)$ provide one or more curves in the plane defined by V_1 and V_2. These curves are denoted as: $H_\eta(V_1,V_2)$. They have been traced in red Fig. 9(a). Solution points must correspond to intersections of D_η and H_η, which can be calculated thanks to the fine tuning enabled by the frequency sweep. In the plane defined by V_1 and V_2, each point of the curves $D_\eta(V_1,V_2)$ and $H_\eta(V_1,V_2)$ corresponds to a distinct frequency ω. Only intersections at the same ω constitute solution points, which is verified through a simple error condition.

In the case of Fig. 9(a), only four intersections occur in the plane V_1 and V_2 between $D_\eta(V_1,V_2)$ and $H_\eta(V_1,V_2)$. Two of them correspond to actual solution points as shown in Fig. 9(b) and Fig. 9(c), where D_η and H_η are traced in terms of V_1 and V_2 versus the frequency ω. The solution points are clearly distinguished.

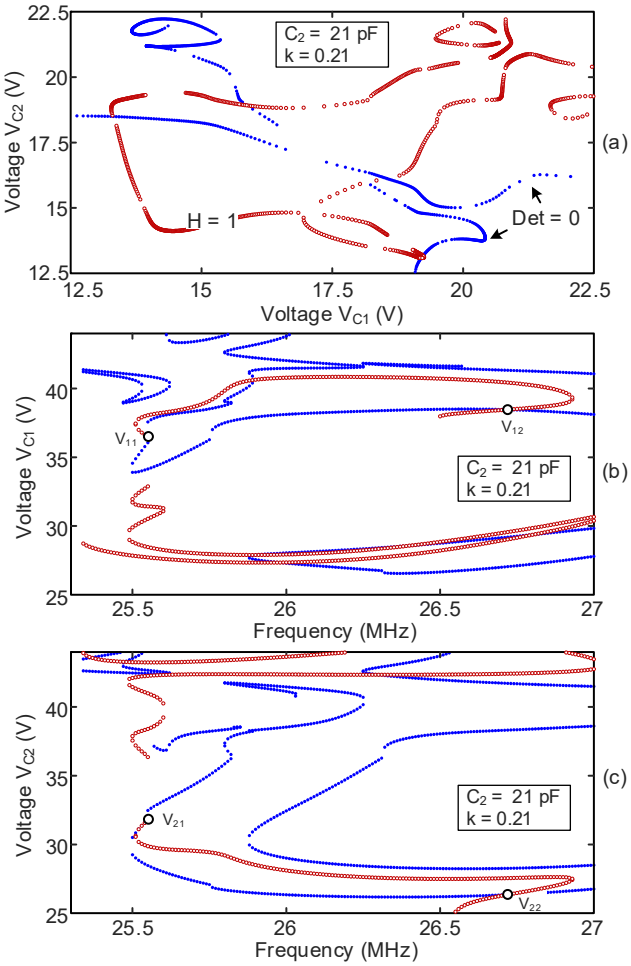

Fig. 9. Numerical method applied to the coupled transistor-based system in Fig. 1(b). Procedure to calculate the solution curves using conditions (18) and (24). (a) Curves $C_\eta^1(V_1,V_2)$ and $C_\eta^2(V_1,V_2)$ for $k = 0.21$. (b) Curves C_η^1 and C_η^2 in the plane ω, V_1 (c) Curves C_η^1 and C_η^2 in the plane ω, V_2. (d) Solution curves obtained by assembling the solution points resulting for each $\eta = C_1$.

Now variations in the parameter η will be considered. In the case of the two coupled differential oscillators of Fig. 1(b), this parameter corresponds to the capacitance C_1 in the first oscillator. Fig. 10 presents a family of solution curves versus variations in the capacitor C_1 for different values of the coupling factor k. Fig. 10 presents the resulting evolution of the oscillation frequency. Comparing with the results of the analytical formulation in Section III, one obtains the same qualitative behaviour. For small k [Fig. 10(a)] there are two pairs of disconnected curves, as in the case of Fig. 4. For better clarity, only the upper-amplitude closed curve has been represented, skipping the lower amplitude curves. For very small k (0.05), the closed curve exhibits two turning points only [Fig. 10(a)-(b)], as in Section II. For $k = 0.1$, a small loop appears in the upper section of this curve, so there are four turning points. As k is further increased, the closed curves split and each section merges with one of the open curves, to give rise to an open solution curve [Fig. 10(c)]. For each k, there are two open curves, one for each mode. As shown in Fig. 10(d), the phase shift ϕ exhibits a strong variation through the closed solution curves, where it goes from -180º to 180º. This phase shift varies in a limited range after the curve merging, as shown in Fig. 10(c).

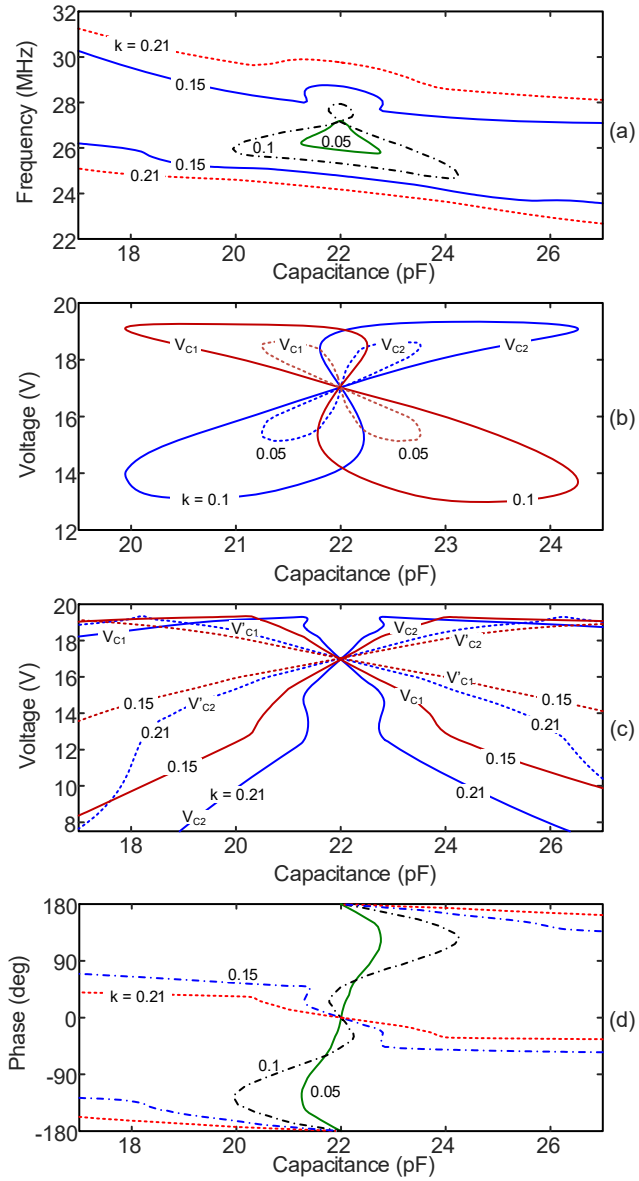

Fig. 10. Numerical method applied to the system of two inductively-coupled transistor-based oscillators in Fig. 8(a)-(b). Evolution of the solution curves versus the capacitor C_1 with the coupling factor. (a) Frequency. (b) Amplitude under low k. (c) Amplitude under higher k (c) Phase shift.

The solution predicted by the numerical technique has been compared with experimental measurements. With this aim, the coupling factor k of the two coupled differential oscillators has been estimated from the measurement of the scattering matrix of the coupled inductors. The resulting value is $k = 0.21$. Fig. 11(a) and Fig. 11(b) present a comparison of the predicted and measured variations of the oscillation amplitudes and phase shift versus the capacitor C_1. The measurement points exhibit a good agreement with the analysis results corresponding to one of the oscillation modes. Fig. 11(c) presents the phase-noise spectrum obtained with the conversion-matrix approach [50] at $C_1 = 22$ pF. The results are compared with the experimental characterization using the R&S® FSWP8 Phase Noise

Analyzer. Both in simulations and measurements the phase-noise spectrum is compared with the one obtained in uncoupled conditions (standalone operation). An improvement of about 3 dB is obtained, in agreement with the theory.

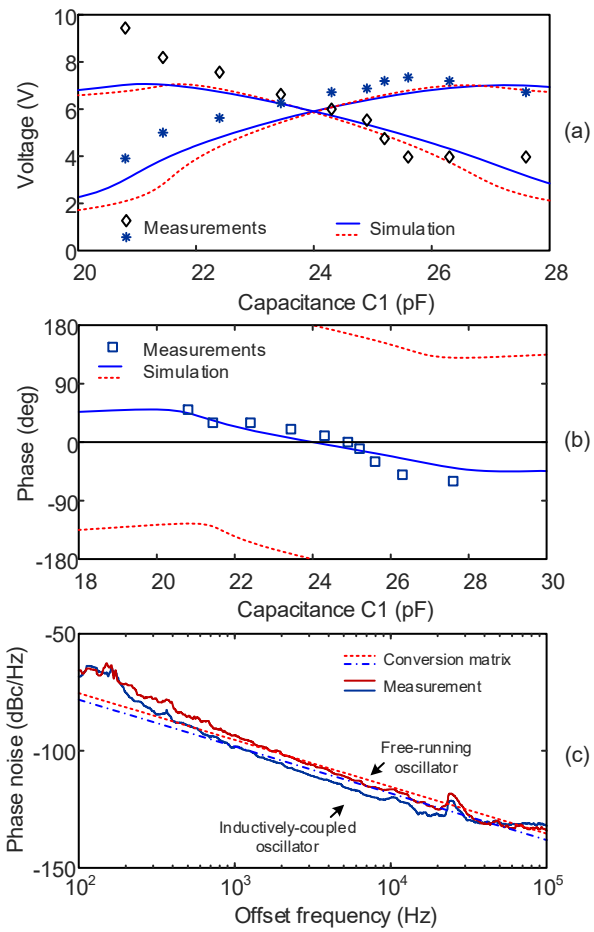

Fig. 11. Coupled transistor-based system. The experimentally characterized coupling factor is $k = 0.21$. Comparison of the predicted and measured variations of the oscillation frequency, amplitudes and phase shift versus the capacitor C_1.

The two periodic modes obtained for $k = 0.21$ are stable, with different basins of attraction. Fig. 12 presents time-domain simulations and experimental measurements, demonstrating the physical coexistence of the two modes. The basin of attraction of one of the modes is much larger than that of the other, so the out-of-phase mode was rarely observed in practice. Note that there can be situations in which only one of the modes is stable. This will happen, for instance, if only one the four sections (delimited by the turning points) of the original eight-shaped curve is stable.

V. Coupling at the Frequency Ratio 1:*N*

The nonlinear analysis of two mutually injection-locked oscillators at the ratio 1: N is more involved than the one at 1:1, considered in Section III. To formulate the system, coupling effects are considered at the resonance frequency $N\omega$, corresponding to the fundamental frequency of the higher-frequency oscillator. Thus, the fundamental component of the first oscillator is only affected by the second oscillator through the coupling of its harmonic component V_N at $N\omega$. Assuming injection-locked operation at ω, the system is described as:

$$Y_{T,1}(V_1, V_N, \phi, \omega) = 0 \qquad \text{(a)}$$

$$\left\{ \begin{bmatrix} Y_{A,N}(V_1, V_N, \phi, N\omega) & 0 \\ 0 & Y_{A,b}(V_b, N\omega) \end{bmatrix} + \begin{bmatrix} y_{p11} & y_{p12} \\ y_{p21} & y_{p22} \end{bmatrix} \right\} \begin{bmatrix} V_N \\ V_b e^{j\alpha} \end{bmatrix} = 0 \qquad \text{(b)}$$

(25)

where $Y_{T,1}$ is the total admittance function of the lower-frequency oscillator at its fundamental frequency, $Y_{A,N}$ is the nonlinear active admittance function of this oscillator at the harmonic frequency $N\omega$, $Y_{A,b}$ is the nonlinear active admittance function of the higher-frequency oscillator at $N\omega$ and y_{pij} are parameters of the admittance matrix of the coupling network, which may include additional linear elements. Its dependence on (ω, k, η) has been dropped for simplicity. The phase origin is set at the Nth harmonic component of the first oscillator, so V_N is real.

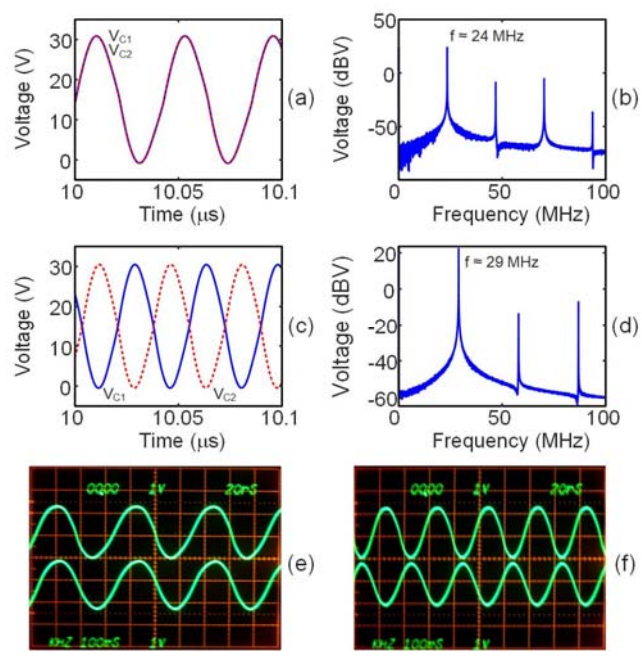

Fig. 12. Coexistence of stable modes demonstrated with time-domain simulations and measurements. (a) and (c), waveforms in equivalent nodes of the two oscillators resulting from time-domain simulations under different initial conditions. (b) Spectrum corresponding to (a). (d) Spectrum corresponding to (c). (e) Measured waveforms: in-phase solution. (f) Measured waveforms: out-of-phase solution.

The equation $Y_{T,1} = 0$ in (25)(a) can be taken as a constraint when addressing the coupled system (25)(b). This can be done by extracting the admittance function $Y_{A,N}(V_1, V_N, \phi, \omega)$ under the fulfillment of $Y_{T,1} = 0$. If the oscillator at ω has good

convergence properties in standalone (non-coupled) operation, the function $Y_{A,N}(V_1,V_N,\phi,\omega)$ can be calculated by introducing two AGs into this oscillator, one at ω (AG_1) and the other at $N\omega$ (AG_2). The AG_2 is not optimized but used as an excitation source to calculate the admittance $Y_{A,N}(V_1,V_N,\phi,\omega)$. A double sweep is performed in ϕ and V_N, optimizing V_1 and ω at each step in order to fulfill $Y_{T,1}=0$. The function $Y_{A,N}(V_1,V_N,\phi,\omega)$, calculated under the constraint $Y_{T,1}=0$, will be introduced in (25)(b). If the oscillator at ω does not exhibit good convergence properties, the function $Y_{A,N}(V_1,V_N,\phi,\omega)$ can be obtained using the method in [26] for the calculation of synchronized-solution curves in a single injection-locked oscillator. Thus, extracting $Y_{A,N}(V_1,V_N,\phi,\omega)$ should not be a problem.

The procedure to solve (25)(b) is identical to the one described in Section III. The search for solution points of (25)(b) must be performed using the function $Y_{A,N}(V_1,V_N,\phi,\omega)$ calculated in the previous analysis and the pairs of values V_N and ω must be limited to those resulting from that analysis. The values of V_N and ω constitute a near conic surface. Instead, the points V_b, ω have not limitation and define a plane.

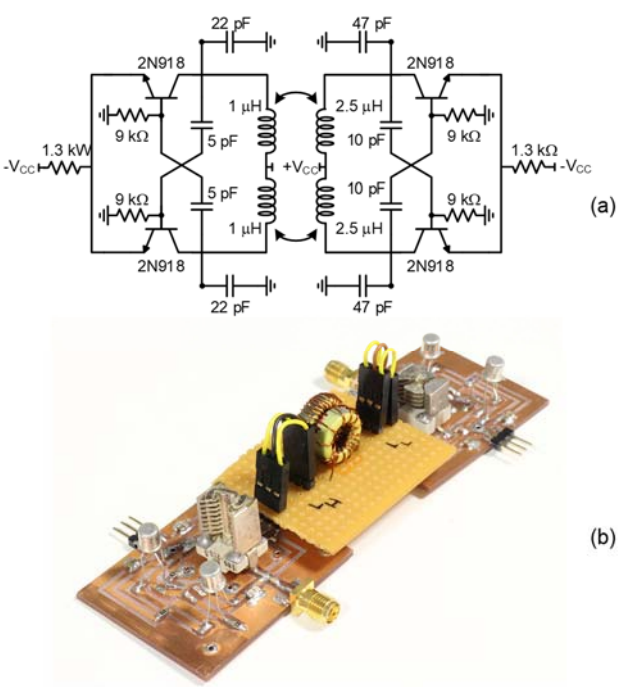

Fig. 13 Coupled oscillator system with two differential transistor-based oscillators at the ratio 1:3. (a) Schematic. (b) Photograph.

The method has been applied to analyze the system in Fig. 13, coupled at the ratio 1:3. When isolated from each other, the two circuits oscillate at the respective frequencies 10 MHz and 30 MHz. Fig. 14(a) presents the near conic surface in the space defined by V_1, V_3 and ω. The "unfolded" surface in the space defined by V_3, ω and ϕ is shown in Fig. 14(b). The solution curves obtained through (25) are shown in Fig. 15. In this figure, the voltage amplitude in one of the oscillators, the synchronized oscillation frequency ω and the phase shift ϕ have been represented versus the capacitance in the higher-frequency oscillator for different k values. For the implementation shown in Fig. 13(b), the coupling factor estimated from the measurement of the scattering parameters of the coupled inductors is $k = 0.15$. Fig. 16(a) and (b) present before and after synchronization when varying C_1. Fig. 16(c) presents the phase-noise spectrum of the oscillator at 30 MHz, experimentally characterized with the R&S® FSWP8 Phase Noise Analyzer, in both coupled and free-running operation.

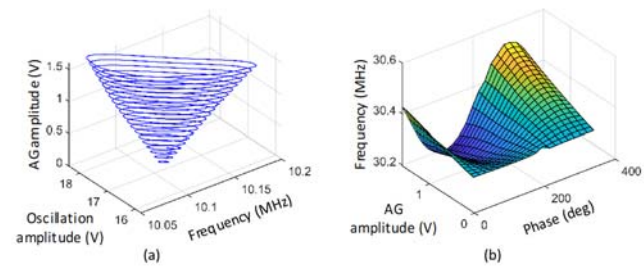

Fig. 14. Analysis of the system of two coupled differential oscillators at the frequency ratio 1:3 shown in Fig. 13. (a) Near conic surface in the space defined by V_1, V_3 and ω. (b) "Unfolded" surface in the space defined by V_3, ω and ϕ.

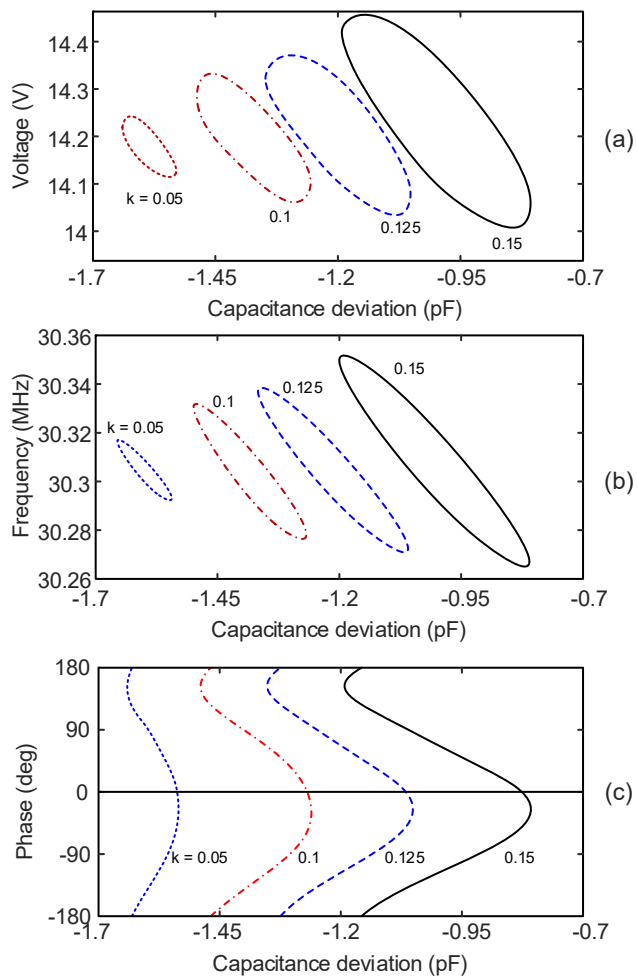

Fig. 15. Solution curves obtained through (26) for k = 0.05, 0.1, 0.125 and 0.15. (a) Voltage amplitude in one of the collectors of the 30 MHz oscillator, (b) Synchronized oscillation frequency, and (c) phase shift. The three magnitudes have been represented versus the capacitance deviation with respect to their free-running value.

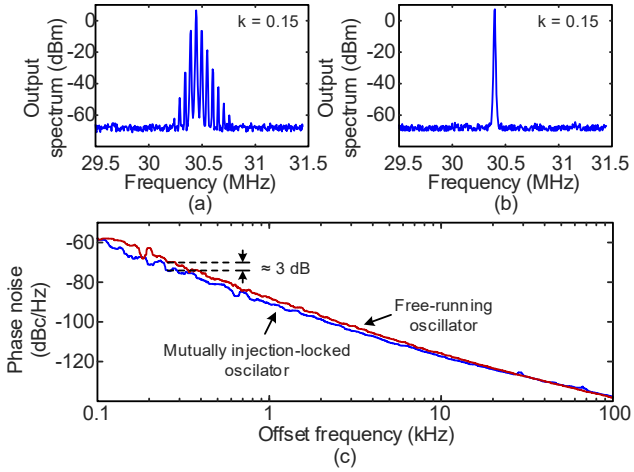

Fig. 16. Measured spectrum of the coupled oscillator system shown in Fig. 13 for k = 0.15. (a) Spectrum prior to the synchronization. (b) Synchronized spectrum. The capacitance and frequency are in agreement with the results shown in Fig. 14(b). (c) Phase-noise spectrum of the oscillator at 30 MHz, experimentally characterized with the R&S® FSWP8 Phase Noise Analyzer.

VI. Conclusion

An in-depth investigation of the operation of two inductively coupled oscillators under strong coupling conditions has been presented. This is based on an analytical formulation of the coupled system, and the behavior pattern obtained when increasing the coupling factor has been found to be general and thus also observed in realistic transistor-based oscillators. Under the bilateral injection locking, one obtains two distinct families of solutions curves, one corresponding to each major operation mode. For the lower values of the coupling factor one obtains a closed solution curve and two open curves, which, for a higher coupling factor merge into two distinct curve families. A numerical method has also been developed for the realistic analysis of coupled transistor-based oscillators, which enables an exhaustive detection of all the coexisting oscillation modes. The method tackles the system equations in an original way that enables the use of contour-intersection techniques. The numerical method has been successfully extended to the case of oscillator coupling at the frequency ratio 1:N. This requires the extraction of the model of the lower frequency oscillation under the constraint of the fulfillment of the oscillation condition at its fundamental frequency. The methods have been applied to two pairs of coupled transistor-based oscillators at different frequency ratios and very good results have been obtained in comparison with the measurement results.

References

[1] V. Issakov, J. Rimmelspacher, S. Trotta, M. Tiebout, A. Hagelauer R. Weigel, "A 52-to-67 GHz dual-core push-push VCO in 40-nm CMOS," *47th European Microwave Conference (EuMC),* Nuremberg, 2017.

[2] J. Rimmelspacher, R. Weigel, A. Hagelauer, V. Issakov, "A Quad-Core 60 GHz Push-Push 45 nm SOI CMOS VCO with −101.7 dBc/Hz Phase Noise at 1 MHz offset, 19 % Continuous FTR and −187 dBc/Hz FoMT," *IEEE European Solid State Circuits Conf.*, Dresden, 2018, pp. 138-141.

[3] D. Murphy, H. Darabi, "A 27-GHz Quad-Core CMOS Oscillator With No Mode Ambiguity," *IEEE J. Solid-State Circuits*, vol. 53, no. 11, pp. 3208-3216, 2018.

[4] C. Sideris, P. P. Khial, A. Hajimiri, "Design and Implementation of Reference-Free Drift-Cancelling CMOS Magnetic Sensors for Biosensing Applications," *IEEE J. Solid-State Circuits,* vol. 53, pp. 3065-3075, 2018.

[5] J. Rimmelspacher, R. Weigel, A. Hagelauer and V. Issakov, "36% Frequency-tuning-range dual-core 60 GHz push-push VCO in 45 nm RF-SOI CMOS technology," *2017 IEEE MTT-S International Microwave Symposium (IMS)*, Honolulu, HI, 2017, pp. 1356-1358.

[6] Y. Shu, H. J. Qian, X. Luo, "A 169.6-GHz Low Phase Noise and Wideband Hybrid Mode-Switching Push–Push Oscillator," *IEEE Trans. Microw. Theory Techn.*, vol. 67, no. 7, pp. 2769-2781, July 2019.

[7] V. Issakov, F. Padovan, "A Dual-Core 60 GHz Push-Push VCO with Second Harmonic Extraction by Mode Separation," *IEEE Radio Frequency Integrated Circuits Symposium (RFIC)*, Philadelphia, PA, 2018, pp. 208-211

[8] FY. Shu, H. J. Qian and X. Luo, "A 169.6 GHz Hybrid Mode-Switching Push-Push Oscillator with 21.7% Tuning Range and 180.6dBc/Hz FoMT in 28nm CMOS Technology*," 2018 IEEE/MTT-S International Microwave Symposium - IMS*, Philadelphia, PA, 2018, pp. 1423-1426.

[9] G. Li, L. Liu, Y. Tang and E. Afshari, "A Low-Phase-Noise Wide-Tuning-Range Oscillator Based on Resonant Mode Switching," *IEEE J. Solid-State Circuits,* vol. 47, no. 6, pp. 1295-1308, June 2012.

[10] J. Chien and A. M. Niknejad, "Oscillator-Based Reactance Sensors With Injection Locking for High-Throughput Flow Cytometry Using Microwave Dielectric Spectroscopy", *IEEE J. Solid-State Circuits*, vol. 51, no. 2, pp. 457-472, Feb. 2016.

[11] J. Juillard, P. Prache and N. Barniol, "Analysis of Mutually Injection-Locked Oscillators for Differential Resonant Sensing," *IEEE Trans. Circuits and Systems I: Regular Papers*, vol. 63, no. 7, pp. 1055-1066, July 2016.

[12] M. Ferrari, V. Ferrari and K. K. Kanazawa, "Dual-harmonic oscillator with frequency and resistance outputs for quartz resonator sensors," *SENSORS, 2008 IEEE*, Lecce, 2008, pp. 1261-1264.

[13] S. Rong and H. Luong, "Analysis and design of transformer-based dualband vco for software-defined radios," *IEEE Transactions on Circuits and Systems I*: *Reg. Papers,* vol. 59, no. 3, pp. 449–462, Mar. 2012.

[14] J. Pan, A. A. Abidi, W. Jiang, D. Marković, "Simultaneous Transmission of Up To 94-mW Self-Regulated Wireless Power and Up To 5-Mb/s Reverse Data Over a Single Pair of Coils," *IEEE J. Solid-State Circuits*, vol. 54, no. 4, pp. 1003-1016, 2019.

[15] H.-C. Chang, X. Cao, U. Mishra, R. York, "Phase noise in coupled oscillators: Theory and experiment", *IEEE Trans. Microw. Theory and Techn.*, vol. 45, no. 5, pp. 604- 615, May 1997.

[16] S. Sancho, A. Suárez, J. Domínguez, F. Ramírez, "Analysis of near carrier phase noise spectrum in free-running oscillators in the presence of white and colored noise sources," *IEEE Trans. Microw. Theory Techn*, vol. 58, no. 3, pp. 587-601 , Mar., 2010.

[17] K. Kurokawa, "An Analysis of Rucker's Multidevice Symmetrical Oscillator," *IEEE Trans. Microw. Theory Techn.*, vol. 18, pp. 967-969, 1970.

[18] F. Ramírez, M. Pontón, S. Sancho, A. Suárez, "Stability analysis of oscillation modes in quadruple-push and Rucker's oscillators," *IEEE Trans. Microw. Theory Techn.*, vol. 56, no. 11, pp. 2648-2661, Nov., 2008.

[19] M. Pontón, A. Suárez, *"*Oscillation Modes in Symmetrical Wireless-Locked Systems*," IEEE Trans. Microw. Theory Techn*., vol. 66, no. 5, pp. 2495-2510, May, 2018.

[20] A. Suárez, F. Ramirez, R. Melville, "Mutual injection locking of oscillator circuits through inductor coupling," *IEEE MTT-S International Microwave Symposium*, Los Angeles, USA, 2020.

[21] A. Suarez, F. Ramirez and S. Sancho, "Stability and Noise Analysis of Coupled-Oscillator Systems," *IEEE Trans. Microw. Theory Techn.*, vol. 59, no. 4, pp. 1032-1046, Apr. 2011.

[22] A. Suarez, S. Sancho, and F. Ramirez, "General formulation for the analysis of injection-locked coupled-oscillator systems," *IEEE Trans. Microw. Theory Tech.*, vol. 61, no. 12, pp. 4730–4744, Dec. 2013.

[23] F. Ramirez, M. E. de Cos and A. Suarez, "Nonlinear analysis tools for the optimized design of harmonic-injection dividers," *IEEE Trans. Microw. Theory Techn.*, vol. 51, no. 6, pp. 1752-1762, June 2003

[24] F. Ramírez, M. Pontón, S. Sancho, A. Suárez, "Phase−Noise Analysis of Injection−Locked Oscillators and Analog Frequency Dividers", *IEEE Trans. Microw. Theory Techn.*, vol. 56, no.2, pp. 393−407, 2008.

[25] M. Pontón, A. Suárez, "Wireless injection locking of oscillator circuits," IEEE Trans. Microw. Theory Techn., vol. 64, no. 12, pp. 1-15, Dec., 2016.

[26] S. Sancho, M. Pontón, A. Suárez, "Effects of Noisy and Modulated Interferers on the Free-Running Oscillator Spectrum," *IEEE Trans. Microw. Theory Techn.*, vol. 66, no. 4, pp. 1831-1842, Apr., 2018.

[27] P. Liao and R. A. York, "A new phase-shifterless beam-scanning technique using arrays of coupled oscillators", *IEEE Trans. Microw. Theory Techn.*, vol. 41, no. 10, pp. 1810-1815, Oct. 1993.

[28] T. Heath, "Simultaneous beam steering and null formation with coupled, nonlinear oscillator arrays", *IEEE Trans. Antennas and Propagation*, vol. 53, no. 6, pp. 2031-2035, June 2005

[29] A. Suárez, *Analysis and Design of Autonomous Microwave Circuits*. Hoboken, NJ: Wiley IEEE Pres, 2009.
[30] E. F. Calandra and A. M. Sommariva, "Stability Analysis of Injection-Locked Oscillators in Their Fundamental Mode of Operation", *IEEE Trans. Microw. Theory Techn.*, vol. 29, no. 11, pp. 1137-1144, Nov. 1981.
[31] J. Guckenheimer and P. Holmes, *Nonlinear Oscillations, Dynamical Systems, and Bifurcations of Vector Fields*. New York, NY, USA: Springer-Verlag, 1990.
[32] J. M. T. Thompson and H. B. Stewart, *Nonlinear Dynamics and Chaos*, 2nd ed. Hoboken, NJ, USA: Wiley, 2002.
[33] E. Ngoya and R. Larchèveque, "Envelop transient analysis: A new method for the transient and steady state analysis of microwave communication circuits and systems," *IEEE MTT-S Int. Microw. Symp. Dig.*, San Francisco, CA, USA, Jun. 1996, pp. 1365–1368.
[34] E. de Cos, A. Suárez and S. Sancho, "Envelope transient analysis of self-oscillating mixers," *IEEE Trans. Microw. Theory Techn.*, vol. 52, no. 4, pp. 1090-1100, April 2004,
[35] S. Hernández, A. Suárez, "Envelope-Domain Analysis and Modeling of Super-Regenerative Oscillators," *IEEE Trans. Microw. Theory Techn.*, vol. 66, no. 8, pp. 3877-3893, Aug., 2018.
[36] F. Ramirez, J. L. Garcia H, T. Fernandez and A. Suarez, "Nonlinear simulation techniques for the optimized design of push-push oscillators," *IEEE MTT-S International Microwave Symposium Digest*, 2003, Philadelphia, PA, USA, 2003, pp. 2157-2160 vol.3.
[37] J. de Cos, A. Suárez, "Efficient Simulation of Solution Curves and Bifurcation Loci in Injection-Locked Oscillators," *IEEE Trans. Microw. Theory Techn.*,vol. 63, no. 1, pp. 181-197, Jan. 2015.
[38] S. Hernández, M. Pontón, A. Suárez, "Simulation Method for Complex Multivalued Curves in Injection-Locked Oscillators," *IEEE Trans. Microw. Theory Techn.*,vol. 65, no. 11, pp. 4046-4062, Nov. 2017.
[39] E. L. Allgower and K. Georg, *Introduction to Numerical Continuation Methods*. Philadelphia, PA, USA: SIAM, 2003.
[40] W. Rheinboldt and J. Burkardt, "Algorithm 596: A program for a locally parameterized continuation process," *ACM Trans. Math. Softw.*, vol. 9, no. 2, pp. 236–241, 1993.
[41] L. T. Watson, S. C. Billups, and A. P. Morgan, "Algorithm 652: HOMPACK: A suite of codes for globally convergent homotopy algorithms," ACM Trans. Math. Softw., vol. 13, no. 3, pp. 281–310, Sep. 1987.
[42] R. Quere, E. Ngoya, M. Camiade, A. Suarez, M. Hessane and J. Obregon, "Large signal design of broadband monolithic microwave frequency dividers and phase-locked oscillators," *IEEE Trans. Microw. Theory Techn*., vol. 41, no. 11, pp. 1928-1938, Nov. 1993.
[43] A. Suárez, R. Quéré, *Stability Analysis of Nonlinear Microwave Circuits*. Artech House, Norwood (Ma), Jan. 2003.
[44] J. Jugo, J. Portilla, A. Anakabe, A. Suarez, J. M. Collantes, "Closed-loop stability analysis of microwave amplifiers*," Electronics Letters*, vol. 37, no. 4, Mar, 2001, pp. 226-228.
[45] J. Jugo, J. Portilla, A. Anakabe, A. Suárez, and J. M. Collantes, "Closed-loop stability analysis of microwave amplifiers," *IEE Electronics Letters*, vol. 37, no. 4, pp. 226–228, Feb. 2001.
[46] A. Anakabe, J. M. Collantes, J. Portilla, et al. "Analysis and elimination of parametric oscillations in monolithic power amplifiers," *2002 IEEE MTT-S Int. Microwave Symp. Dig*., Seattle, WA, Jun. 2002, pp. 2181–2184.
[47] V. Rizzoli and A. Neri, "State of the art and present trends in nonlinear microwave CAD techniques," *IEEE Trans. Microw. Theory Techn*.,vol. 36, no. 2, pp. 343-365, Feb. 1988.
[48] J. de Cos, A. Suarez and F. Ramirez, "Analysis of Oscillation Modes in Free-Running Ring Oscillators", *IEEE Trans. Microw. Theory Techn*., vol. 60, no. 10, pp. 3137-3150, Oct. 2012.
[49] A. Röhm, K. Lüdge, I. Schneider, *Bistability in two simple symmetrically coupled oscillators with symmetry-broken amplitude- and phase-locking*, Chaos: An Interdisciplinary Journal of Nonlinear Science, Volume 28, Issue 6, Jun. 2018.
[50] V. Rizzoli, F. Mastri and D. Masotti, "General Noise Analysis of Nonlinear Microwave Circuits by the Piecewise Harmonic-Balance Technique," *IEEE Trans. Microw. Theory Techn*., vol. 42, pp. 807-819, May 1994.

Almudena Suárez (M'96–SM'01–F'12) was born in Santander, Spain. She received the Licentiate degree in Electronic Physics and the Ph.D. degree from the University of Cantabria, Santander, Spain, in 1987 and 1992, respectively, and the Ph.D. degree in Electronics from the University of Limoges, Limoges, France, in 1993.

She is currently a Full Professor with the Communications Engineering Department, University of Cantabria. She co-authored *Stability Analysis of Nonlinear Microwave Circuits* (Artech House, 2003) and authored *Analysis and Design of Autonomous Microwave Circuits* (IEEE-Wiley, 2009). Prof. Suárez is an member of the Technical Committees of the IEEE Microwave Theory and Techniques Society (IEEE MTT-S) International Microwave Symposium (IMS) and the European Microwave Conference. She was an IEEE Distinguished Microwave Lecturer from 2006 to 2008. She is a member of the Board of Directors of the European Microwave Association. She was the Coordinator of the Communications and Electronic Technology Area for the Spanish National Evaluation and Foresight Agency between 2009 and 2013. In 2014 and 2015 she was the co-chair of IEEE Topical Conference on RF Power Amplifiers (PAWR). Prof. Suárez is an Associate Editor of the IEEE Transactions on Microwave Theory and Techniques and the IEEE Microwave Magazine.

Franco Ramírez (S'03-A'05-M'05-SM'16) obtained the Licentiate degree in electronic systems engineering degree from the Military School of Engineering (EMI) in La Paz, Bolivia, in 2000 and the Ph.D. degree in Communications Engineering from the University of Cantabria, Santander, Spain in 2005. From 1999 to 2000, he worked for Ericsson de Bolivia Telecomunicaciones, where he was involved in projects related with GSM and TDMA technologies. From 2009 to 2013, Dr. Ramírez was a Research Fellow of the "Ramón y Cajal" Programme, funded by the Spanish Ministry of Science and Innovation, at the Communications Engineering Department of the University of Cantabria, where he is currently an Associate Professor. His research interests include phase noise, stability and the development of nonlinear techniques for the analysis and design of autonomous microwave circuits.

Robert Melville received a B.S. degree in Computer Science from the University of Delaware in 1978 and the Ph.D. in the same subject from Cornell University in 1981. From 1981 to 1984 he was a junior faculty member at the Johns Hopkins University in Baltimore, MD. In 1985 he joined Bell Laboratories, where he worked on computer-aided design and numerical simulation for electronic circuits. In 1994 he was made Distinguished Member of Technical Staff for his work on efficient simulation of large non-linear circuits. He then transferred to a research group working on wireless design under Dr. Mihai Banu. In 2003, he took a position as a Senior Lecturer in the department of Electrical Engineering at Columbia University where he taught graduate and undergraduate courses in circuit design and electronic measurement. Dr. Melville has served as a referee for IEEE Transactions on CAD, IEEE Transactions on Circuits and Systems, the IEEE Journal of Solid-State Circuit and numerous other professional publications. In the spring of 2002, he co-organized a conference on numerical circuit simulation at Sandia Laboratories. He is also extra-class radio amateur WB3EFT.